spectroscopy journal

MDPI

Article

Spectroscopic Characterization of Graphene Oxide Fractions: A Preliminary Step Towards Fabric Functionalization

Andrea Dali [1], Cosimo Bartolini [1,2], Nicola Calisi [3,4], Stefano Cicchi [1], Gabriella Caminati [1,2] and Maurizio Becucci [1,4,5,*]

[1] Department of Chemistry "Ugo Schiff" (DICUS), University of Florence, Via della Lastruccia 3, I-50019 Sesto Fiorentino, FI, Italy; andrea.dali@unifi.it (A.D.); cosimo.bartolini.98@gmail.com (C.B.); stefano.cicchi@unifi.it (S.C.); gabriella.caminati@unifi.it (G.C.)
[2] Center for Colloid and Surface Science (CSGI), University of Florence, Via della Lastruccia 3, I-50019 Sesto Fiorentino, FI, Italy
[3] Department of Industrial Engineering (DIEF), University of Florence, Via di Santa Marta 3, I-50139 Firenze, FI, Italy; nicola.calisi@unifi.it
[4] National Interuniversity Consortium of Materials Science and Technology (INSTM), Via Giuseppe Giusti 9, I-50121 Firenze, FI, Italy
[5] European Laboratory for Non-Linear Spectroscopy (LENS), Via Nello Carrara 1, I-50019 Sesto Fiorentino, FI, Italy
* Correspondence: maurizio.becucci@unifi.it

Abstract

Flexible electronic textiles hold potential applications across various fields, yet current functionalization methods frequently suffer from poor coating uniformity and severe aesthetic alteration. This study addresses these challenges by establishing a multi-analytical approach, based on Raman spectroscopy together with DLS, Zeta potential and XPS measurements, to optimize graphene oxide (GO) precursor selection prior to electrostatic deposition onto cotton fabrics using a polyethyleneimine linker. This coating strategy was inspired by layer-by-layer deposition technique and centrifugation was used to partition a heterogeneous commercial GO precursor into three distinct homogeneous fractions. Raman spectroscopy revealed that centrifugation acts not merely separating GO based on its size but effectively sorts GO sheets based on their chemical functionalization degree. Consequently, this approach allows for the identification of the optimal precursor fraction, balancing sheet dimensions with defect density, to ensure strong functionalization. Overall, this work established a foundational spectroscopic methodology for precursor selection, deposition monitoring and process optimization, which can also be extended to the characterizing and comparison of different commercial GO batches from different industrial suppliers. Finally, micro-Raman mapping and XPS were preliminary applied to verify the textile fiber functionalization.

Keywords: Raman spectroscopy; micro-Raman spectrometer; XPS; DLS; graphene; graphene oxide; functionalized textiles; e-textiles

Academic Editor: Grazia Giuseppina Politano

Received: 24 July 2026
Revised: 19 August 2026
Accepted: 22 August 2026
Published: 26 August 2026

1. Introduction

Flexible and fibrous textile fabrics enriched with conductive materials are attracting growing interest for their use in a wide range of applications, particularly in electronic textiles (e-textiles) [1–4]. E-textiles are fabrics that enable the incorporation of digital, electronic, and computing components. To impart conductive capabilities to textiles, various conductive or semiconductive materials are typically used. Conductive fabrics

can be manufactured using metallic wires or metallic fibers blended with textile fibers. However, since both metals and traditional semiconductors are rigid materials, they are not particularly suitable for applications on textile fibers, as these are subjected to a high degree of stretching and bending during use. Consequently, there is a growing interest in flexible semiconductive e-textiles made by impregnating textile materials with conductive polymers, such as carbon black, carbon nanotubes, or metal-based powders [1].

Among conductive materials, graphene is one of the most used thanks to its outstanding electrical, photothermal and mechanical properties [5]. Graphene is a two-dimensional, non-polar material consisting of a monolayer of sp^2-hybridized carbon atoms organized in a hexagonal structure with conjugated covalent bonds between adjacent carbon atoms [5–9]. The delocalization of π electrons within the hexagonal lattice makes graphene a strong, thin, and flexible material with excellent thermal and conductive properties [10–12]. For example, graphene-treated textiles can be used to produce waterproof and ultraviolet radiation shielding textiles due to both its strong hydrophobicity and effective absorption of solar radiation [13–18]. However, the interaction between graphene and cotton is challenging and, therefore, it is preferred to use derivatives of graphene [19,20]. Among those, an important derivative is graphene oxide (GO), graphene's oxidized form, which maintains the graphene hexagonal structure but introduces oxygenated functional groups (Figure 1). GO is applied onto fabrics to increase their mechanical strength and thermal comfort while simultaneously imparting antibacterial and antistatic properties (Figure 1) [13,21,22]. Furthermore, the presence of hydroxyl, carboxyl, and epoxide groups makes GO highly dispersible in water and, therefore, readily applicable on textiles. Altogether, GO and related graphene-based nanomaterials have demonstrated widespread potential across different fields, ranging from flexible fabrics to electrochemical energy storage devices, electrocatalysts and biomedical applications [13,23–29]. However, the structural defects in GO and the presence of oxygen groups disrupt the conjugated network, turning GO into an inherently insulating material [24,30].

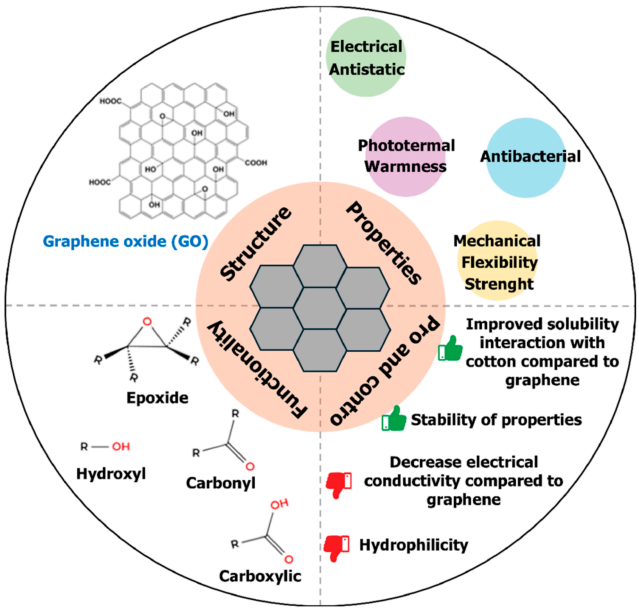

Figure 1. Summary of the characteristics of graphene oxide (GO) with its structure, functional group, advantages and disadvantages and useful properties for application in fabric production. Adapted from Refs. [24,25].

Another key derivative of graphene is reduced graphene oxide (rGO). Chemical reduction of GO is commonly used for its preparation, allowing for the density of functional

groups to be tuned according to the specific needs of the application [24,25]. While GO acts as an electrical insulator due to the breaking of the sp^2 network by oxygen-containing groups, its subsequent reduction to rGO can restore electrical conductivity. The straightforward processability of GO and the conductivity of rGO make these materials perfect candidates for the development of smart and conductive textiles. Therefore, optimizing the preliminary deposition of GO is a mandatory step before any reduction process aimed at developing e-textiles.

To date, various techniques exist for functionalizing fabrics with graphene and its derivatives [1]. However, these processes often rely on multi-step protocols and expensive reagents, and result in coatings that are not uniform. Moreover, all these techniques deposit large amounts of materials onto the textile fibers, which results in a dark coloration (e.g., black with graphene or brown with GO) [13–15]. To overcome these limitations and minimize the aesthetic alteration of the textiles, we are working to explore the deposition of an ultra-thin layer of GO that should be nearly transparent but sufficiently stable and well-anchored to the cotton. Cotton was chosen as the target textile substrate due to its widespread relevance, eco-compatibility and distribution.

The surface of GO presents electron-rich hydroxyl groups that provide an ideal functionalization point. Specific and strong interactions can be obtained through an electrostatic approach by exploiting the negative surface charge of cotton to anchor graphene via electrostatic interactions. Since both cotton and GO expose negative charges at neutral pH [18,31,32], it is necessary to introduce a third element to act as a mediator to establish an attractive interaction. For this purpose, polyethyleneimine (PEI), a cationic polyelectrolyte, was used. PEI is particularly suitable because (i) it exposes positive charges at neutral pH, promoting interaction with both cotton and graphene; (ii) it is transparent, thus not altering the appearance of the fabric; (iii) it is water-soluble, allowing for easy application by immersing the fabric in an aqueous PEI solution; (iv) it improves the homogeneity of the cotton surface by reducing its roughness, a key factor for uniform deposition. This electrostatic deposition strategy is inspired by the principles of the layer-by-layer (LbL) deposition technique, where alternating layers of oppositely charged species can be sequentially deposited [33–36]. Moreover, this approach opens the possibility of future optimization through the controlled deposition of multiple PEI/GO bilayers, enabling the fine-tuning of the material properties according to the specific requirements of different applications [29,37–39].

Previous results [40] demonstrated how homogeneous monolayers of graphene oxide on silicon oxide and copper surfaces could be achieved by isolating optimally sized populations. Here, we adopted the same protocol to separate fractions of graphene oxide with varying sizes and low polydispersity, in line with recent efforts demonstrating the critical role of controlled GO size fraction [41]. Recently, this approach was also successfully employed to develop an anticorrosion coating for heritage metals and coins [42].

In this paper, we will focus on the application of Raman spectroscopy to guide the optimization of the precursor selection to obtain uniform GO-functionalized fabrics without altering their color or structural integrity, and then to investigate the intermediate steps and final products. Raman spectroscopy represents a non-destructive fundamental tool for evaluating the quality and the number of layers of graphene materials by means of characteristic peaks whose intensity, shape, and position are sensitive to structural and physicochemical parameters [9,43]. In particular, Raman spectroscopy allows for the monitoring of doping, defects, strain and edges [44–50]. Defects (i.e., anything that breaks the symmetry of the lattice, like edges, grain boundaries, change in carbon hybridization, vacancies, implanted atoms) have an effect on the properties of the material and, therefore, it is essential to investigate them [51–53]. The strongest band in the Raman spectrum of

graphene satisfies the Raman selection rules [54]; however, other Raman-forbidden bands are activated when the periodic lattice of graphene is broken, as in GO, by the presence of defects [55]. The activation of these defect-activated bands and their position, relative intensities and shape provide useful information related to graphene quality [56].

To provide a comprehensive characterization of the system, Raman spectroscopy was combined with other techniques, such as dynamic light scattering (DLS), Zeta potential measurements and X-ray photoemission spectroscopy (XPS). By combining these spectroscopic techniques, this study establishes a quantitative, predictive methodology that connects microscopic with macroscopic interfacial assembly behavior. Moreover, this work will critically discuss the importance of Raman spectroscopy and detailed multi-peak deconvolution models in optimizing precursor selection and assembly strategies for functionalized textile fabrics, decoupling the interfacial assembly challenges from downstream chemical treatments.

2. Materials and Methods

2.1. Graphene Preparation and Textiles Functionalization

Raw organic cotton fabrics were pre-treated in a 4% water NaOH solution for 60 min at 80 °C. This process is similar to industrial mercerization and aims to remove potentially fluorescing contaminants present on the fibers (like stains or optical whiteners). Generally, mercerization requires the use of concentrated NaOH solutions (30% *w*/*v*) [57]; however, in this work, it was decided to follow the protocol described in Ref. [13] to have a lower impact on the fibers.

After mercerization, the fabrics were functionalized using PEI (polyethylenimine, average molecular weight 25,000 g/mol, branched, Merck KGaA, Darmstadt, Germany) and a dispersion of graphene oxide (GO) (Merck KGaA, Darmstadt, Germany) in water (0.5–4 mg/mL). In particular, the cotton was functionalized with PEI by immersing it in a 0.2 g/L aqueous solution (25 mL–pH 9) and heating at 90 °C for 30 min. The cotton was then washed with 25 mL of an aqueous solution containing 2 g/L Triton X-100 and 0.2 g/L Na_2CO_3 at 90 °C for 15 min, as described in Ref. [58]. Finally, it was rinsed with a 0.2 g/L Na_2CO_3 solution, and the fabric was dried in an oven at 60 °C. After drying, the cotton was stored in a vacuum desiccator. Before application, the water dispersion of GO was sonicated for 30 min to obtain a homogeneous and stable dispersion. Then, the fiber was immersed for 30 min at room temperature in the GO dispersion. Finally, the fiber was washed in water and let dry in an oven at 90 °C.

The GO dispersions were centrifuged using a benchtop centrifuge (NEYA 16R, Neya Centrifuges, Carpi, MO, Italy) equipped with an S4-175 swing-out rotor fitted with B 2-50R buckets for 50 mL round-bottom tubes. The centrifugation was repeated twice to achieve the best possible separation of the three different GO fractions. In particular (Figure S1): (i) the precipitate collected from the first centrifugation step contains the largest fraction of GO particles and was named Ultra-Large Graphene Oxide (ULGO); (ii) the precipitate collected from the second centrifugation step contains the intermediate-sized fraction, named Large Graphene Oxide (LGO); (iii) the remaining supernatant contains the smallest fraction, called Small Graphene Oxide (SGO).

2.2. Preliminary Characterization of GO Dispersions and Fractions

The aqueous dispersions of GO were investigated by using a Zetasizer PRO (Malvern Panalytical Ltd., Worcestershire, England, UK) to determine the dimensions of the graphene sheets via dynamic light scattering (DLS) and the stability of the dispersion by measuring the Zeta potential. Moreover, the morphology of the GO sheets was investigated by optical

microscopy (Nikon Diaphot 300, Tokyo, Japan) by depositing the aliquots onto a glass microscope slide.

2.3. Raman Spectroscopy

Raman analysis was conducted at room temperature on few drops of the water–GO dispersion (for GO fraction) or on single fibers (for fabrics) using a micro-Raman spectrometer RM2000 (Renishaw, Wotton-under-Edge, UK) equipped with 20×/0.40 N.A. Olympus microscope objective and a 514 nm argon ion laser (Spectra Physics, Milpitas, CA, USA). The samples were put on a computer-controlled motorized stage (accuracy 1 μm) and investigated using a laser power on the sample of 50 μW, to avoid structural damage. The Raman spectra wavenumber scale was routinely calibrated on the 520 cm^{-1} first-order Raman band of bulk silicon: wavenumber accuracy along the full spectrum is 2 cm^{-1} and the spectral resolution is 5 cm^{-1}. For each sample, at least 50 individual points were characterized by Raman spectroscopy (acquisition time 20 s at each spot), taking care to explore different regions in a randomized way, and spectra were averaged, to increase the signal to noise ratio. To better evaluate all the bands, a fitting analysis was performed by using a free software package (Fityk 1.3.1) including a cubic baseline function and a set of four bands in the spectral region of fundamental transitions (1100–1900 cm^{-1}) and three bands in the region of combination and overtone transitions (2350–3450 cm^{-1}), respectively [59].

It has to be noted that different functions (Lorentzian, Gaussian, pseudo-Voight) are used to fit graphene Raman spectra [56,60–64]. The functions used were determined, during analysis, to be the better fit. Two other bands are expected in the GO Raman spectrum (assigned as D* at 1100 cm^{-1} and G* at 2500 cm^{-1}, according to Ref. [56]) but were too small to be detected in our Raman spectra, also upon spectral deconvolution.

In the case of GO the presence of D″ and D* bands (~1180 cm^{-1}) affects the I_D/I_G ratio [56]. For this reason, in accordance with Ref. [56], the ratio between the D and G bands was evaluated on the fitted bands.

2.4. X-Ray Photoelectron Spectroscopy

X-ray photoelectron spectroscopy (XPS) investigation was performed on fabric cut and fixed using a graphitic double-sided adhesive tape and then, installed in an ultra-high vacuum (UHV) XPS analysis chamber. The instrument used an X-ray source nonmonochromatic (VSW Scientific Instrument Limited, Manchester, England, UK, model TA10, Mg Kα radiation, 1253.6 eV) with a power of 120 W (12 kV and 10 mA). The analyzing chamber is equipped with a hemispherical analyzer (VSW Scientific Instrument Limited, model HA100, Manchester, England, UK) mounting a 16-channel detector and operating in fixed pass energy mode (44 eV). A differential pumping stage allows for operating down to a pressure of 5×10^{-8} mbar in the main chamber.

Spectra were analyzed using a dedicated software package (CasaXPS, Version 2.3.25PR1.0, CasaSoftware Limited, Teignmouth, UK) to remove the inelastic background according to the Shirley's method [65]. A deconvolution of the XPS spectra was carried out using a combination of Gaussian and Lorentzian components. The binding energy scale was calibrated using adventitious carbon as an internal reference, with the C 1s peak set at 284.8 eV [66].

2.5. Water Contact Angle (WCA) Measurement

Water wettability was assessed using an Automated Contact Angle Goniometer (Ramé-Hart, Inc., Mountain Lake, NJ, USA) equipped with a fiber-optic light source, to minimize evaporation effects, and a CCD camera, for capturing high-resolution images. A computer-controlled dispenser (Auto Pipetting System, Ramé-Hart Inc., Mountain Lake, NJ, USA)

delivered 5 µL droplets. Both left and right contact angles were determined via software-assisted image analysis every 5 s until reaching spreading equilibrium. The fabric samples were attached with masking tape at the ends and fixed onto a glass microscope slide so that the fabric was taut, providing a completely flat and horizontal surface on which to deposit the droplet.

2.6. Generative Artificial Intelligence (GenAI)

In this paper, generative artificial intelligence was used only to assist in the technical refinement of data interpretation. Specifically, GenAI assisted in ensuring precise analysis of data for the analytical discussion. No data generation, text generation, analysis generation, graphics manufacturing or study designs were performed by the AI. The final intellectual evaluation and analysis remain entirely with the authors.

3. Results

3.1. Optimization of the GO Fractions

3.1.1. Preparation of GO Fractions

To improve the reproducibility and uniformity of the coating process, the bulk GO dispersion was preliminarily fractionated by centrifugation, allowing for the separation of GO sheets according to their lateral dimensions. This approach was built on a previous study on GO based protective coatings [42], which demonstrated that the coating process benefits from the size selection of graphene oxide sheets, promoting a more homogeneous and controlled deposition onto a given substrate. The commercial GO precursor was divided into three fractions (Figure S1—see Section 2): ultra-large graphene oxide (ULGO); large graphene oxide (LGO); small graphene oxide (SGO).

3.1.2. DLS Characterization of GO Fractions

For effective assembly onto textile fibers, maintaining a well-dispersed state within the aqueous medium is fundamental; otherwise, rapid colloidal aggregation would compromise the coating uniformity. Therefore, the separated GO fractions were first investigated by light scattering techniques to (i) obtain information regarding the apparent size of the GO sheets in the various fractions via DLS measurements, (ii) evaluate the stability of the dispersion via Zeta potential measurements. Number-weighted size distributions were considered to better describe the particle populations in each sample, while the average hydrodynamic diameters were obtained from the intensity-weighted distributions.

The LGO and SGO fractions exhibited well-defined populations with average hydrodynamic diameters of 875 and 594 nm, respectively (Figure 2 and Table 1). These values should be considered as approximate estimates, since DLS analysis assumes spherical particles and provides the hydrodynamic diameter, which also includes the contribution of the hydration layer surrounding the GO sheets. Therefore, the measured sizes do not correspond directly to the actual lateral dimensions of the GO sheets. However, in a previous study based on a similar centrifugation procedure [42], SEM analysis of the different GO fractions revealed sheet dimensions consistent with the DLS size ranges observed in the present work.

Table 1. Z-average dimensions (nm) and polydispersity index (PDI) of the LGO and SGO fractions.

Fraction	PDI	Average Dimensions (nm)
LGO	0.35 ± 0.02	875 ± 37
SGO	0.42 ± 0.05	594 ± 24

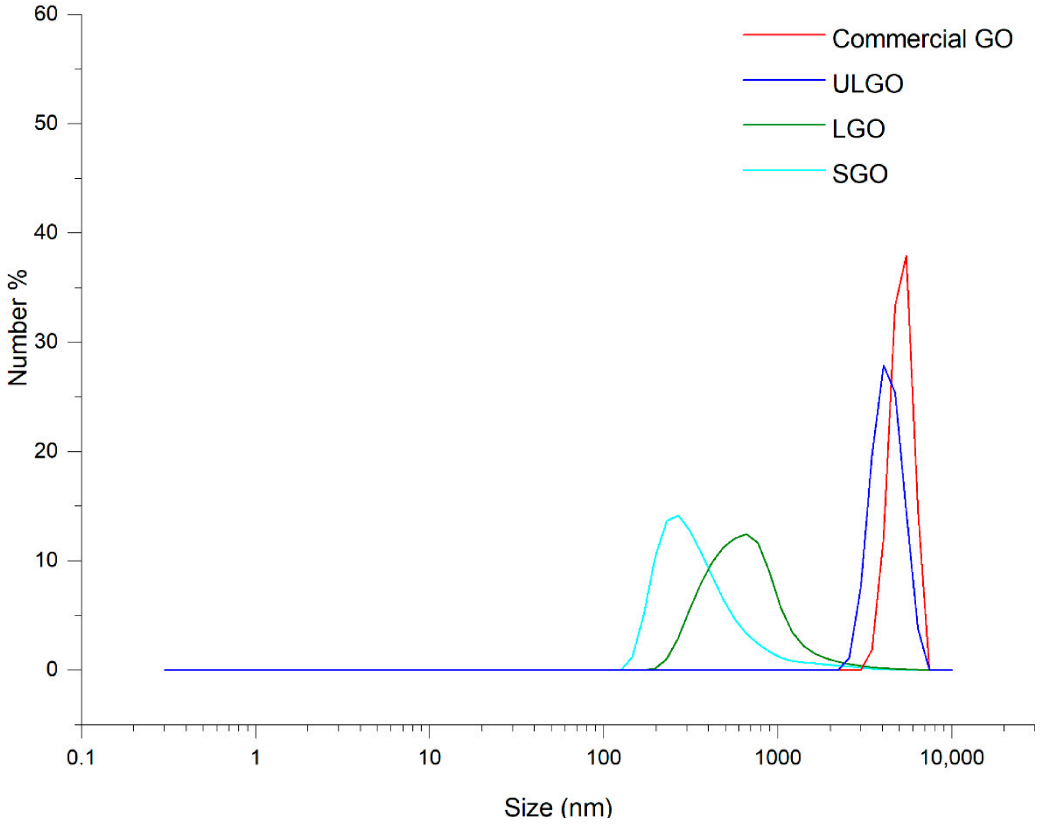

Figure 2. Number-weighted size distribution for the different fractions of the GO dispersions and the commercial GO.

Differently, the DLS profiles of the raw GO dispersion and the freshly resuspended ULGO fraction were very similar (Figure 2), both showing a broad population of very large GO sheets whose characteristic size exceeded the upper detection limit of the instrument and therefore could not be determined exactly. The apparent sharp feature for both ULGO and the raw commercial GO in Figure 2 is an artifact caused by the instrument's upper size detection limit, which truncates the broad, polydisperse distribution of ultra-large sheets present in the unseparated bulk precursor. Therefore, we report in Table 1 only the data for LGO and SGO. When the ULGO dispersion was allowed to stand for approximately 10 min after resuspension, the largest sheets sedimented and the remaining supernatant showed a population with average dimensions (514 nm) comparable to those of the LGO and SGO fractions (Figure S2). This result indicates that the centrifugation process does not produce a complete separation of the GO sheets according to their size, and that the different fractions partially overlap. Moreover, the rapid sedimentation of the largest sheets demonstrates the poor colloidal stability of the ULGO fraction. As a result, the composition of the dispersion changes over time, making this fraction unsuitable for achieving a homogeneous and reproducible coating of the cotton substrate.

Moreover, Zeta potential analyses of the three fractions at various concentrations (Figure 3), compared to that of the commercial GO, allow for the determination of the exposed surface charge, which provides crucial information on the stability of the aqueous dispersions. The obtained Zeta potential values range from −30 to −50 mV. Generally, if the Zeta potential exhibits value higher than +30 mV or lower than −30 mV the dispersion can be classified as highly stable [67]. In fact, under these conditions, the electrostatic repulsion forces between adjacent particles are strong enough to overcome attractions and they will prevent the nano- or micro-particles from aggregating. This analysis, therefore, confirms the outstanding stability of the aqueous GO dispersions. The negative potential

values indicate that the particles expose a negative surface charge, primarily due to the deprotonation of the carboxylic and hydroxyl groups present on the edges and planes of the GO sheets, which occurs at neutral pH values.

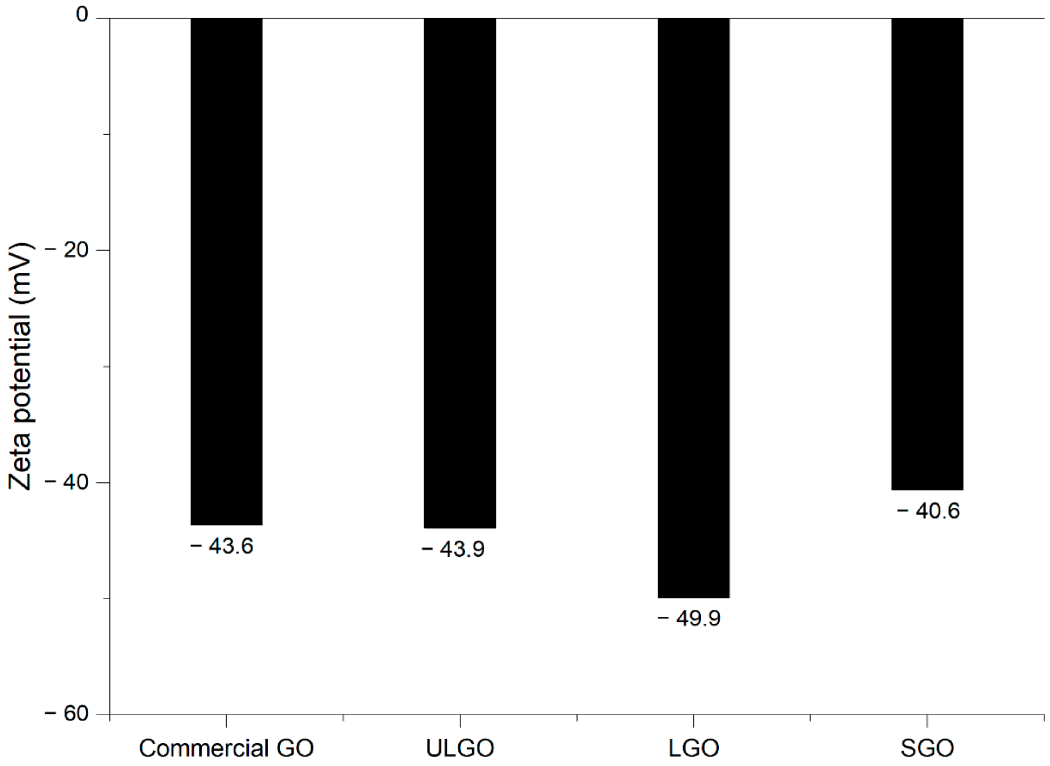

Figure 3. Zeta potential of the various ULGO, LGO, and SGO fractions compared to that of the commercial GO.

3.1.3. Raman Characterization of GO Fractions

The interpretation and assignment of the Raman bands of graphene are well-known [9,44,46,54,60,68,69], whereas the situation for GO is more complicated due to the presence effects of defects and the presence of heteroatoms/different functional groups [56,70]. In this study, each GO fraction was characterized by micro-Raman spectroscopy, combined with curve-fitting analysis, mainly according to Refs. [56,70].

In the Raman spectra of GO, we expected an intense band around 1582 cm^{-1} (G band) resulting from in-plane C-C stretching vibrations [54]. This band is present in all graphitic materials containing a network of sp^2 carbon atoms [54] but its position (ω_G), which is generally unaffected by the excitation wavelength used, varies with the number of layers (n) [71]. As the thickness (associated with the number of layers n) increases, the G band tends to shift to lower wavenumbers. It should be emphasized, however, that other factors also influence the position and shape of this band, such as temperature, doping (both electron and hole), and strain. At 1350 cm^{-1} the D band is observed [47,54]. This band, resulting from the ring breathing mode of sp^2 carbon atoms, is directly linked to the presence of defects in the crystal lattice of the sample. In fact, this band is Raman-forbidden, and it is not observed in pristine graphene samples: it is only activated by the presence of defects. Its intensity increases when the number of defects in the sample increases, making it an extremely sensitive indicator of the sample's structural quality [56]. The position (ω_D) is dependent on the excitation wavelength used. The ratio between the intensities of the D and G bands (I_D/I_G) is commonly used to estimate the degree of disorder in graphene materials [47,56,71]. In the specific case of GO, the oxidation introduces oxygen groups that represent defects. Therefore, this ratio gives information related to its reduction degree [72].

According to the Ferrari classification, for low-defect systems (stage 1), the I_D/I_G ratio is less than 3.5, while for highly disordered systems (stage 2), the ratio is greater than 3.5 [56,60]. This value was obtained at an excitation energy of 2.41 eV for a mean distance within defects of 3–5 nm [60]. When the number of defects increases significantly, the D band broadens and weakens because of the C_{sp2} ring break, causing a decrease in the I_D/I_G ratio. For this reason, it is always important to also evaluate other parameters, such as the full width at half maximum (FWHM) of the G and D bands. In fact, samples at different stages can exhibit the same I_D/I_G ratio but a very different FWHM(D), with the latter being larger in stage 2.

Another band activated in the presence of defects is the D′ band (1620 cm^{-1}). The intensity ratio $I_D/I_{D'}$ allows for distinguishing point defects (vacancies, sp^3-hybridized carbon atoms) from extended structural defects (edges, grain boundaries, line defects) [53]. In particular, higher values of this ratio are associated with defects related to sp^3 hybridization of carbon atoms, whereas the ratio decreases for vacancies and reaches its minimum for boundary-like defects. These experimental relationships reflect the sensibility of D′ band intensities (1620 cm^{-1}) to different types of defects [53].

Another important aspect to evaluate for samples within stage 1 of amorphization is the linearity between the relative areas of D′, D and G bands, specifically the $A_{D'}/A_G$ versus the A_D/A_G ratios. The slope of this correlation line (i.e., the ratio $A_{D'}/A_D$) depends on the primary type of defect dominant in the sample (vacancies, sp^3-hybridized carbon atoms, grain boundaries) [68]. More specifically, this ratio is approximately 0.14 for vacancies, 0.08 for sp^3-defects, and 0.29 for grain boundaries [53,73,74].

At 2685 cm^{-1}, the second harmonic of the D band (2D or G′ band) is reported [54,56]. Unlike the G band, this peak always satisfies the Raman selection rules via a double-resonance process and, therefore, it is always observed for graphene and its derivatives [56]. The line shape of the 2D band is related to the number of graphene layers: for graphene monolayers it is a single Lorentzian with FWHM of ~24 cm^{-1}; for graphene with more than one layer, this band can be decomposed into several Lorentzian components; for turbostratic graphene (i.e., monolayer of graphene stacked in a completely random way), the 2D band is a single peak but with a high FWHM. Moreover, the position of this band depends on the excitation wavelength used. The intensity ratio between the intensities of the 2D and G peaks (I_{2D}/I_G), the Raman shift of the peaks (ω_{2D} and ω_G), and their shape are used as qualitative parameters to estimate the number of layers [60,69]. In particular, the I_{2D}/I_G ratio for graphene is generally (i) greater than 2 for monolayers (1-LG), (ii) equal to 1 in bilayers (2-LG), and (iii) drops below unity in samples with a higher number of layers [56].

There are also weaker bands that are activated in the presence of defects, such as the D″ band (1500–1550 cm^{-1}), 2D′ band (3500 cm^{-1}), or the D + G band (2940 cm^{-1}) [44,45,54,56,68]. The position of the D″ band reflects the oxygen content of GO [56] and the crystallinity of GO [70]. Moreover, the $I_{D''}/I_G$ ratio decreases as the crystallinity of the GO sheets increases [56].

Following the above discussion, we started to model the Raman spectrum of commercial GO spectrum using four bands in the spectral region of the fundamental transitions (1100–1900 cm^{-1}) and three bands in the spectral region of combination and overtones (2350–3450 cm^{-1}) as reported in Figure 4 and Table 2. We have identified the different spectral components as follows: D band (1352 cm^{-1}), D″ (1543 cm^{-1}), G band (1592 cm^{-1}), D′ (1616 cm^{-1}), 2D band (2710 cm^{-1}), D + G band (2930 cm^{-1}), and 2D′ band (3170 cm^{-1}). It has to be noted that the assignment of the D + G band was reported as uncertain in the literature. However, in our case, the wavenumber fits very well with the sum of the frequencies of the D and G bands, supporting the given assignment. It should be also

noted that, even if the band centers are clearly determined, the shape of the experimental spectrum is not perfectly reproduced using this model. We repeated the fitting process to the Raman spectra of the separated GO fractions (Figure 4 and Table 2). The position of the D″ and D + G bands remains identical to that observed in commercial GO. On the other hand, we have a slight shift in the D (1343–1352 cm^{-1}), G (1588–1594 cm^{-1}), D′ (1620 cm^{-1}), 2D (2680–2700 cm^{-1}) and 2D′ (3185 cm^{-1}) bands, which points to a difference in the structural configuration of the GO sheets for the different fractions. It is worth noting that the 4 + 3 bands model we applied leads to a very good fit to the experimental data for the different fractions we prepared. Therefore, we conclude that this model is appropriate for the isolated fractions, while it is not fully able to account for the highly heterogeneous size and defect distribution of the bulk commercial precursor.

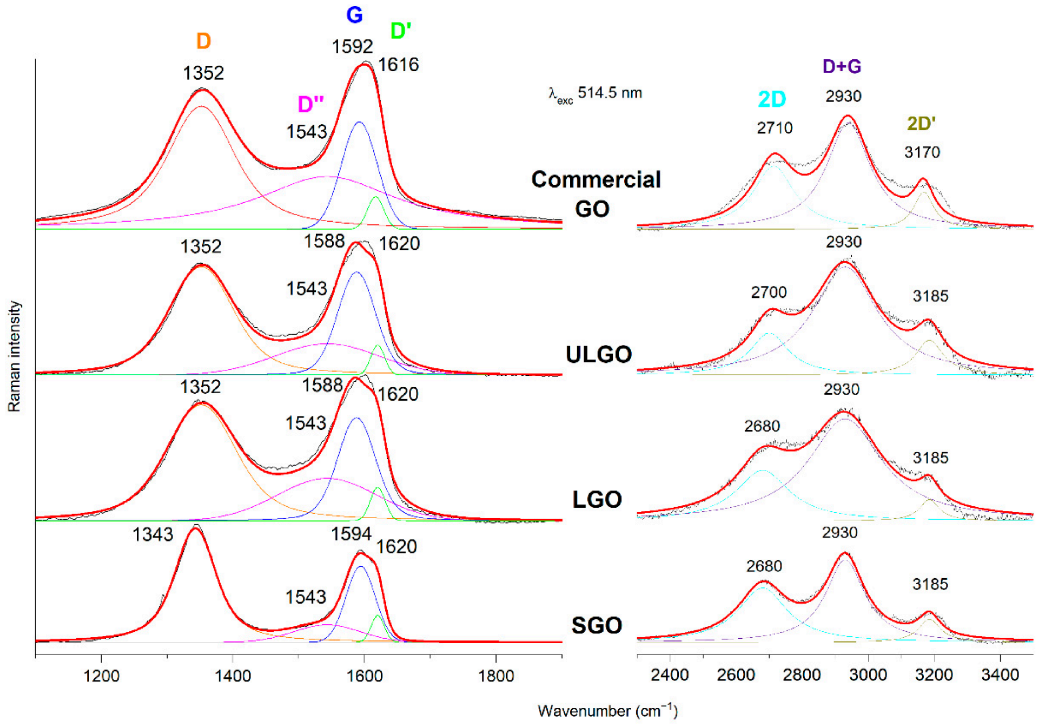

Figure 4. Raman spectrum of the commercial graphene oxide and its fraction (SGO, LGO and ULGO) obtained with the 514.5 nm excitation wavelength. Fitting parameters are reported in Table 2. Deconvolution bands are shown in orange (D), pink (D″), blue (G), green (D′), light blue (2D), purple (D+G), light brown (2D′). The result fitted curve is shown in red.

To gain deeper insight into the structural parameters, the I_D/I_G and $I_D/I_{D'}$ ratios were evaluated (Table 3). SGO exhibits a high I_D/I_G ratio (2.83), indicating a significant overall number of defects and/or reduction degree, although the commercial GO (2.91) presents a slightly higher value. However, the FWHM of the D band for SGO is the lowest among the analyzed compounds (75 cm^{-1}) suggesting less disorder within the remaining sp^2 domains. Furthermore, the $I_D/I_{D'}$ value is high (17.7), implying that the principal kind of defects are connected to sp^3 hybridization of carbon atoms. This agrees with the hypothesis that the oxygen functionalization component is dominant compared to total defects contributing to the D band.

Conversely, LGO and ULGO exhibit a lower I_D/I_G ratio than SGO (2.29 and 2.05, respectively), but this value can be misleading if considered alone. In fact, the FWHM of the D band is much larger than that observed for SGO (127 cm^{-1} for LGO and 116 cm^{-1} for ULGO), suggesting extremely high disorder characterized by the distortion/breaking of aromatic rings and the loss of long-range order. Then, the increase in the $I_D/I_{D'}$ value

(20.2 for LGO and 20.5 for ULGO) shows that the oxygen-bonded component is relatively more significant compared to the amorphous component in the D band. Interestingly, commercial GO presents an I_D/I_G ratio (2.91) very similar to that of SGO, while its $I_D/I_{D'}$ value is the highest among all samples (21.1) suggesting an important contribution of the reduction and oxygen functionalization component.

Table 2. Fitting parameters calculated for commercial GO and the different GO fractions in the first and second order Raman spectra (Figure 4). The second-order bands of commercial GO were not satisfactorily fitted with the model applied (see Figure 4) and the corresponding set of parameters is not reported.

Fraction	D (Voight)			D″ (Voight)			G (Voight)			D′ (Voight)		
	x_c (cm^{-1})	w (cm^{-1})	A (%)	x_c (cm^{-1})	w (cm^{-1})	A (%)	x_c (cm^{-1})	w (cm^{-1})	A (%)	x_c (cm^{-1})	w (cm^{-1})	A (%)
ULGO	1352	116.5	52.1	1543	187.2	20.0	1588	67.9	25.4	1620	24.7	2.5
LGO	1352	127.1	52.5	1543	178.8	22.1	1588	49.3	22.9	1620	26.5	2.6
SGO	1343	75.2	62.6	1543	120.1	11.7	1594	52.0	22.1	1620	23.6	3.6
GO commercial	1352	123.3	42.1	1543	256.2	41.5	1592	64.2	14.4	1616	29.3	2.0
Fraction	**2D (Lorentz)**			**D + G (Lorentz)**			**2D′ (Lorentz)**					
	x_c (cm^{-1})	w (cm^{-1})	A (%)	x_c (cm^{-1})	w (cm^{-1})	A (%)	x_c (cm^{-1})	w (cm^{-1})	A (%)			
ULGO	2700	141.0	16.8	2930	238.2	73.1	3185	101.6	10.1			
LGO	2680	196.6	25.4	2930	270.9	70.6	3185	81.8	14.6			
SGO	2680	180.9	76.2	2930	143.6	9.2	3185	81.8	14.6			

Table 3. Relevant spectroscopic parameters ratio for the SGO, LGO, ULGO, and commercial GO fractions obtained from the Raman spectra (Figure 4).

Fraction	I_D/I_G	$I_D/I_{D'}$	$I_{D''}/I_G$	$I_{D'}/I_G$	I_{2D}/I_G
ULGO	2.05	20.5	0.78	0.09	0.58
LGO	2.29	20.2	0.96	0.11	0.93
SGO	2.83	17.7	0.53	0.16	1.22
GO commercial	2.91	21.1	2.88	0.14	

For all the samples, we observe a single 2D peak with a high FWHM (141.0–196.6 cm^{-1}) suggesting that in all cases the GO was composed of different planes randomly oriented closely resembling the electronic and structural behavior of turbostratic graphene, consisting of carbon planes stacked with complete rotational randomness. Consequently, the standard I_{2D}/I_G ratio (Table 3) used to evaluate the number of layers cannot be strictly applied. The higher value observed for SGO (1.22) do not indicate a monolayer or bilayer thickness, but rather represent a spectral artifact caused by the severe amorphization of the fractions.

Finally, the $I_{D''}/I_G$ ratio reaches its maximum for the raw commercial GO (2.88) confirming a heavily disordered structure with a small crystallinity. On the other hand, the isolated fractions show a significant drop in this parameter (0.96–0.53), suggesting a higher local structural crystallinity with lower incidence of the amorphous carbon phase.

Since all fractions possess an I_D/I_G ratio lower than 3.5, a linear dependence between the $A_{D'}/A_G$ and A_D/A_G ratios is expected according to Ferrari's classification. This behavior was confirmed for SGO, LGO, and ULGO by plotting the relative intensity of the D′ band ($A_{D'}/A_G$) against the relative intensity of the D band (A_D/A_G) (Figure 5). Furthermore, a linear fit revealed an $A_{D'}/A_D$ ratio of 0.067. This value agrees with the expected defects originating from sp^3-hybridized carbon atoms. This confirms that covalent sp^3 functionalization is largely predominant over lattice vacancies, matching the expected

chemical evolution of highly oxidized sheets. On the other hand, the values for the starting commercial GO do not fall on the line identified by the other points; it is hypothesized that this occurs because the raw sample is a complex mixture of defects that are subsequently separated into various fractions.

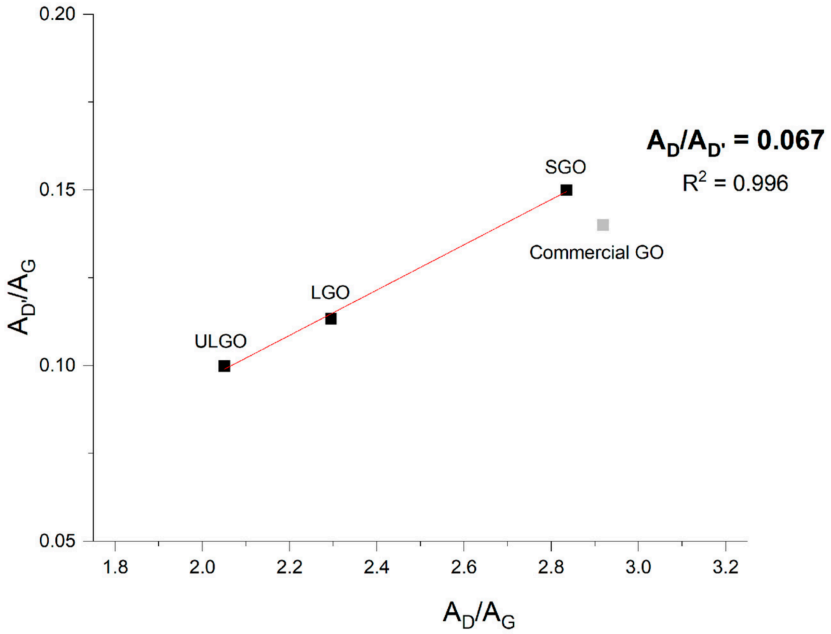

Figure 5. Variations in the relative intensities of the D′ band compared to the D band for the GO fractions (SGO, LGO, and ULGO). Red solid line was obtained by linear fitting the experimental data, in agreement with Ref. [56]. Also, the R^2 value is reported. In gray, the point representative of commercial GO, which does not align with the other data, is also reported.

Moreover, the exact position of the 2D band can be used to estimate the C_{sp2} content (%) [56]. Specifically, using the correlation line (Figure 6), it was possible to estimate a C_{sp2} content of 47% for SGO and LGO, and 71% for ULGO.

Altogether, the Raman investigation is consistent with the process used to obtain individual GO fractions. Indeed, SGO recovered from the supernatant contains the smallest and/or least aggregated GO sheets. Obviously, this implies a greater number of edges per unit volume. Since edges act as defects that activate the D band, this aligns well with a high I_D/I_G ratio and a narrower FWHM(D) due to less amorphization compared to the other fractions. Conversely, since LGO and ULGO are precipitates from centrifugation, they contain larger and/or agglomerated sheets characterized by extreme amorphization, as indicated by the FWHM values. More specifically, LGO exhibits the highest incidence of oxygenated phases, while ULGO is structurally the most complex but also the most restored in terms of graphitic domains. In the case of commercial GO (i.e., the starting material from which the other fractions are separated), it appears to be a heterogeneous and complex mixture of defects that are subsequently partitioned into the various fractions. Furthermore, it can be evaluated that all these fractions are composed of multi-layer GO sheets with a planar organization like that of turbostratic graphite, as indicated by the observation of a single, extremely broad 2D band.

Therefore, centrifugation does not appear to alter or damage the sample; rather, it seems to divide the commercial GO into fractions wherein the thickness of the individual sheets does not vary, but rather the aggregation of the GO sheets and their degree of oxygenation/amorphization do.

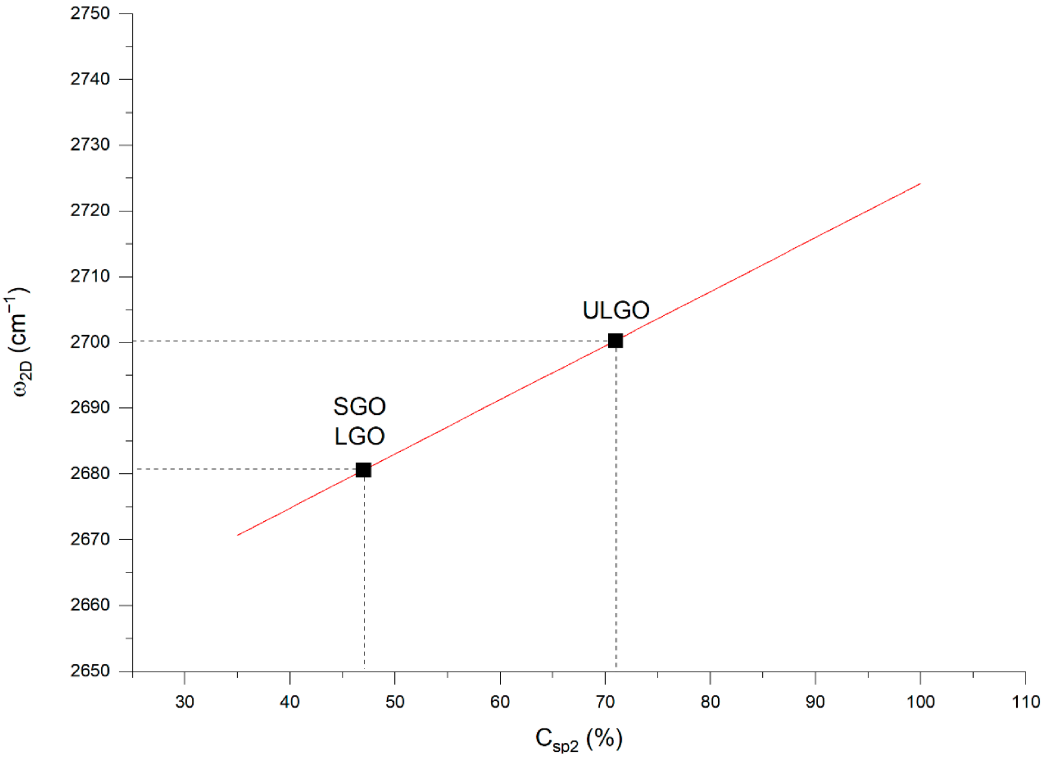

Figure 6. Variations in the position of the 2D band in relation to the C_{sp2} content (%). The red solid correlation line was obtained from Ref. [56].

3.2. Characterization of GO Deposition on Fabrics

3.2.1. Deposition of PEI

In a preliminary way, the functionalization of the textile substrate was investigated. Cotton fabrics, after mercerization, were immersed in a PEI solution (see Materials and Methods). The water contact angle (WCA) of the cotton sample coated with PEI was measured alongside a piece of cotton used as a reference (treated just with NaOH). In both cases, the water droplet was immediately absorbed by the fabric confirming that the PEI functionalization does not significantly alter the wettability of the fabric.

The PEI-coated cotton fabric was studied with Raman spectroscopy, but no Raman signal from PEI was observed. Reference Raman data on PEI [75–77] show Raman peaks for pristine PEI connected with the C=N and C=O stretching and the in-plane bending vibration of CH_2. However, in this case no bands were observed, maybe due to the unfortunate overlap of signals with those of cotton. However, the successful deposition of PEI on the cotton fibers was confirmed by XPS spectroscopy. The N 1s XPS spectra (Figure 7) for the untreated and treated with PEI cotton show that for the cotton sample, not immersed in the PEI solution, the nitrogen signal is weak and corresponds to a tiny atomic fraction (about 0.5%, see Table 4). Such a low percentage can be attributed to impurities present in the cotton or to accidental contamination. On the other hand, in the samples immersed in the PEI solutions, the intensity of the nitrogen signal increases noticeably, and the nitrogen atomic fraction (Table 4) grows to 2.5%. Furthermore, peak fitting allowed for the identification of two distinct components, corresponding to two different nitrogen species. These were identified as N_1 and N_2 with binding energies of approximately 401.7 eV and 400 eV, respectively. The N_2 component, at a lower binding energy, is attributable to nitrogen in a more reduced form, whereas the N_1 component is associated with nitrogen in a more oxidized environment. The N_2 component is prevalent and can be traced back to tertiary amine groups, which represent the main fraction of

the nitrogen units present in the structure of PEI. Conversely, the N_1 component can be attributed to the less abundant primary or secondary amine groups.

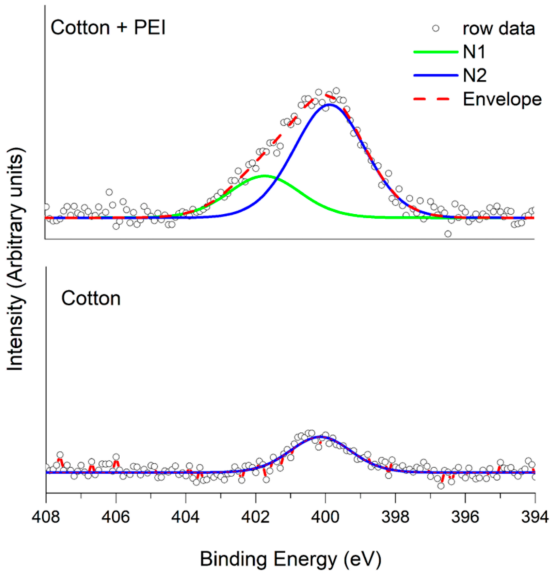

Figure 7. Detail of the XPS spectra characteristic of the 1s nitrogen transition obtained on bare cotton (**bottom**), and after functionalization by immersion in PEI solutions (**top**).

Table 4. Relative atomic percentages of carbon, oxygen, and nitrogen elements. The percentages indicated for the N_1 and N_2 components refer to total nitrogen (Figure 7).

	Pure Cotton	**Cotton Treated with PEI**
C total (%)	66.6	64.0
O total (%)	32.9	33.4
N total (%)	0.5	2.5
N_1 (%)	100	27.0
N_2 (%)	-	73.0

3.2.2. Deposition of GO on PEI-Functionalized Cotton

The cotton treated with PEI was immersed for 30 min in a water dispersion containing LGO at room temperature (see Section 2). The LGO fraction was used for the textile coating as it represents an optimal compromise among all the fractions. In particular, the sheets are large enough to ensure stable and continuous planar coverage over the textile fiber, while retaining a high density of oxygenated functional groups suitable for creating a strong electrostatic interaction with the PEI-functionalized cotton.

After drying, the color of the fabric onto which LGO was deposited showed a slight darkening (Figure 8) confirming that the LGO was adsorbed onto the fabric. Also in this case, the water droplet was immediately absorbed by the fabric, proving that the fabric maintains hydrophilic behavior. Under the microscope, the coating appears homogeneous with no darker and lighter regions across the textile. Raman and XPS analyses (Figure 9) were used in combination to confirm the successful adsorption of GO onto the PEI-coated cotton substrate. The Raman spectra (Figure 9A) exhibited the characteristic bands of both GO and cotton, confirming the presence of the graphene oxide coating. The XPS results (Figure 9B) further demonstrated the successful adsorption of PEI, as evidenced by the characteristic signals associated with secondary and tertiary amine groups.

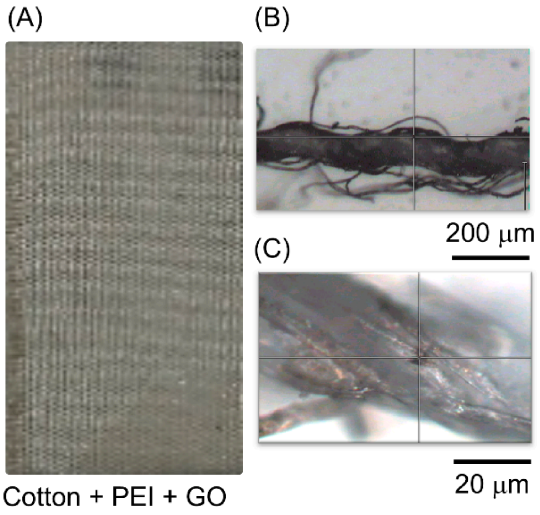

Figure 8. (**A**) Image of the cotton fabric treated with PEI and GO. It was also reported the image of the same sample under the microscope, objective 5× (**B**) and 20× (**C**).

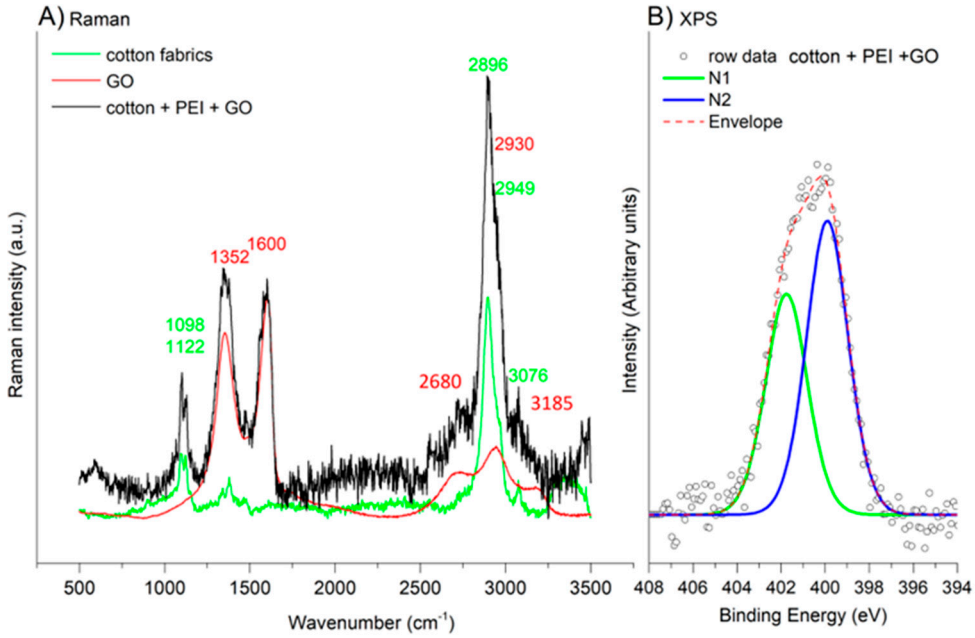

Figure 9. Spectroscopic evidence for the GO functionalization of PEI-coated cotton: (**A**) Raman spectrum of the LGO functionalized cotton fiber (black) compared to the reference clean cotton (green), and pure LGO (red) Raman spectra (all data obtained with 514.5 nm excitation). (**B**) N 1s XPS spectrum of PEI-coated cotton functionalized with LGO (open dots) and the characteristic nitrogen signals associated with nitrogen species in PEI (green and blue traces).

For comparison, the cotton functionalized only with GO was characterized both by visual inspection and Raman spectroscopy. Visually, the resulting deposition was significantly poorer, displaying macroscopic non-homogeneous dark and light spots across the fabric (Figure S3). This expected poor coverage results from mutual electrostatic repulsion between negatively charged cotton fibers and un-primed GO sheets at neutral pH and demonstrated the importance of using PEI as linker. Furthermore, in GO covered areas the Raman spectrum was obtained and resulted similar to those of the PEI-coated functionalized fabrics.

A randomized point micro-Raman mapping across the PEI-LGO functionalized fiber surface demonstrates the homogeneity of the GO deposition on the cotton (Figure S4). Across

all randomly selected spots, the spectra remain consistent, confirming that electrostatic LbL anchoring yields continuous fiber coverage rather than localized aggregate clusters.

Finally, the usage of a higher PEI concentration for the functionalization of cotton was also investigated, but it was found that this yields no benefit. On the contrary, a clear worsening of GO adsorption occurs, as it is adsorbed onto the cotton heterogeneously. A small increase in the I_D/I_G ratio of LGO was observed after deposition with respect to the original material, also potentially related to the absorption only of the more functionalized GO, if damage during the coating process or drying methods cannot be excluded.

4. Discussion

Flexible and fibrous electronic textiles are attracting growing interest in a wide range of applications. Graphene and its derivatives, most notably graphene oxide (GO), its oxidized form, stand out among the most widely used materials. However, conventional techniques used to functionalize fabrics frequently rely on complex multi-step protocols and expensive reagents and frequently result in coatings that are not uniform and have aesthetic alterations.

To overcome these limitations and minimize the aesthetic alteration of the material, we applied a LbL electrostatic deposition method aiming to produce an ultra-thin and stable layer of GO on cotton fibers. Cotton was selected as initial target textile substrate due to its widespread relevance, eco-compatibility and distribution. To achieve robust coating, an electrostatic approach based on the LbL assembly was used by exploiting the negative surface charge of cotton, the cationic polyelectrolyte linker PEI and the negative charge of GO at neutral pH.

The main focus of this work was to demonstrate the utility of Raman spectroscopy in the preparation and characterization of functionalized textile fibers. While Raman spectroscopy represents an essential, non-destructive fundamental and extremely used tool for evaluating the quality and the number of layers of graphene materials, the understanding of Raman spectra for highly disordered GO material is still uncomplete and confused in the literature [56,70]. Therefore, we have made an effort to investigate the usefulness of the different spectroscopic parameters for the characterization of these graphene-based materials. Furthermore, in this paper, Raman spectroscopy was combined with complementary techniques (DLS, Zeta potential measurements and XPS) to provide an in-depth multi-analytical characterization of the systems.

To improve coating reproducibility and uniformity, the commercial GO dispersion was preliminarily fractionated by centrifugation [42]. While centrifugation is traditionally viewed merely as a physical size selection process, our combined DLS and Raman investigation proves that a far more complex role is played by this process. DLS experiment confirmed a dimensional differentiation among the isolated homogenous fraction, with the LGO (875 $\pm$ 37 nm) containing larger particles compared to those of the SGO fraction (594 $\pm$ 24 nm). Conversely, the standard DLS analysis of ULGO fraction yields a low apparent particle size; this is a direct consequence of the rapid sedimentation process that deposits the larger particle populations prior to measurement. Regarding the thickness of each GO sheet, Raman spectroscopy was not able to provide a definitive resolution as in each fraction we prepared GO appears to have a high number of layers with a planar organization similar to that of turbostratic graphite. This is due to the limited sensitivity of Raman spectroscopy with respect to this parameter, with this method, in the case of graphene, only being able to classify materials containing up to 5–10 layers [46,60].

Crucially, micro-Raman spectroscopy investigation coupled with spectral deconvolution revealed that centrifugation effectively separates the sheets based on their distinct chemical functionalization and oxidation degrees. In fact, the fraction isolated from the

supernatant (i.e., SGO) presents the highest I_D/I_G ratio (2.83) coupled with the narrowest FWHM(D) (75.2 cm^{-1}) and the lowest $I_D/I_{D'}$ value (17.7) among all the isolated fractions. This result confirms a population of smaller flakes with a higher density of edge and sp^3 hybridization defects (C_{sp2} content of 47%) yet maintaining a highly preserved crystalline structure.

Conversely, LGO and ULGO display an extreme amorphization of the carbon aromatic rings, as indicated by the smaller I_D/I_G ratio (2.29 and 2.05, respectively) but a significantly broader FWHM(D) values (127.1 and 116.5 cm^{-1}, respectively). Crucially, the increase in the $I_D/I_{D'}$ value (20.2 for LGO and 20.5 for ULGO) compared to SGO demonstrated that the oxygen-bonded component is more significant compared to the amorphous component. In particular, LGO shows the highest incidence of oxygenated functional groups ($I_D/I_{D'}$ 20.2) offering an important contribution of the reduction and oxygen-functionalization component. This multi-analytical approach establishes a powerful predictive tool, allowing for researchers to select specific GO fraction based on both spatial dimensions and specific chemical functionalization.

The analysis of the Raman spectra measured on commercial GO and on the different fractions clearly evidences the heterogeneity of the commercial material through the effectiveness of a simple 4 + 3-band model to reproduce the experimental data in the 1100–1900 cm^{-1} and 2350–3450 cm^{-1} spectral regions. Attempting to deconvolve the first- and second-order Raman spectra of the raw commercial GO using the same number of parameters and peak functions optimized for the fractions (a single band for each know transition) results in a poor mathematical fit of the spectra. This discrepancy arises because bulk commercial GO is a polydisperse, chemically heterogeneous mixture of flakes with varying dimensions and defect types. Consequently, the commercial GO does not fall on the correlation line identified for the other fractions in the AD′/AG vs. AD/AG plot. This mismatch demonstrated that simple models are sometimes insufficient for commercial mixtures that are an ensemble of multidimensional particles with different degrees of structural defects. Therefore, a careful data analysis and/or a multi-analytical approach are always necessary.

For textile functionalization, LGO possibly represents an optimal compromise among all isolated fractions. It balances an appropriate lateral dimension (large enough to bridge the rough textile topography) with the high density of oxygenated groups required for robust electrostatic anchoring onto the PEI-primed cellulose fibers.

Spectroscopic preliminary investigation of the functionalized textile confirms successful interfacial assembly. The deposition of PEI linker was verified via XPS spectroscopy, while Raman analysis clearly confirmed the effective deposition of GO on the fabrics. Moreover, the deposition does not seem to significantly alter the structural integrity of the GO sheets, except for a minor increase in the I_D/I_G ratio. This can be attributed to the selective adsorption of more hydrophilic sheets although minor local restructuring during the drying phase cannot be neglected. Lastly, the micro-Raman mapping definitively proved the uniform distribution of LGO coating across the cotton fabric.

5. Conclusions

This work, by combining Raman spectroscopy with dynamic light scattering (DLS), Zeta potential, and X-ray photoelectron spectroscopy (XPS) techniques, establishes a methodology for precursor selection, deposition monitoring, and process optimization useful for the preparation of functionalized textile fibers. This multi-technique approach has demonstrated that centrifugation does not merely divide commercial GO by lateral sheet dimensions, but effectively sorts sheets based on their oxidation degree and local defect density. Looking at the fraction investigated, we identified LGO as the optimal precursor

for textile functionalization, achieving a balance between sufficient sheet dimensions to cover the irregular fiber surface and a high density of oxygenated binding sites required for strong electrostatic anchoring. Finally, LGO was successfully deposited onto cotton fibers: both optical microscopy and micro-Raman spectra confirmed the formation of a uniform coating across the fabrics.

Furthermore, this multi-analytical framework can be applied for industrial quality control, enabling the differentiation of commercial GO batches from different suppliers. Future research will target post-deposition reduction strategies (either chemical or thermal) to convert the immobilized GO layers into conductive reduced graphene oxide (rGO) for e-textile applications, alongside evaluating coating resilience during standardized mechanical stress and washing procedures.

Supplementary Materials: The following supporting information can be downloaded at https://www.mdpi.com/article/10.3390/spectroscj4030016/s1, Figure S1: Graphical summary of the centrifugation protocol used for the separation of GO fraction; Figure S2: Number-weighted size distribution for ULGO fraction freshly made and after stand for approximately 10 min after separation; Figure S3: Microscope image (objective 5×) of the cotton fabric directly treated with GO (no use of PEI); Figure S4: Micro-Raman spectra of cotton treated with PEI and LGO measured in randomly selected points of the fibers.

Author Contributions: Conceptualization, S.C., G.C. and M.B.; methodology, S.C., G.C. and M.B.; validation, A.D., C.B., G.C. and M.B.; formal analysis, A.D., C.B. and N.C.; investigation, A.D., C.B. and N.C.; resources, S.C., G.C. and M.B.; data curation, A.D., C.B. and N.C.; writing—original draft preparation, A.D. and M.B.; writing—review and editing, A.D., C.B., N.C., S.C., G.C. and M.B.; visualization, A.D. and C.B.; supervision, G.C. and M.B.; project administration, S.C., G.C. and M.B.; funding acquisition, S.C., G.C. and M.B. All authors have read and agreed to the published version of the manuscript.

Funding: This research was funded by the ITALIAN MINISTERO DELLE IMPRESE E DEL MADE IN ITALY (MISE): Studio di applicazioni industriali innovative del grafene, GRAFENEX, progetto 131 Decreto n. 0001481 del 08/05/2023. CUP B53D23025560001.

Institutional Review Board Statement: Not applicable.

Informed Consent Statement: Not applicable.

Data Availability Statement: The data presented in this study are available on request from the corresponding author.

Acknowledgments: We thank S. Caporali (DIEF—University of Florence) for helpful discussion and support. During the preparation of this manuscript, the author used Gemini 1.5 Pro (June 2026 version) for the purposes of ensuring precise analysis of data for the analytical discussion. No data generation, text generation, analysis generation, graphics manufacturing or study designs were performed by the AI. The authors have reviewed and edited the output and take full responsibility for the content of this publication.

Conflicts of Interest: The authors declare no conflicts of interest.

Abbreviations

The following abbreviations are used in this manuscript:

DLS	Dynamic light scattering
e-textiles	Electronic textiles
G-COOH	Graphene functionalized with carboxylic group
G-NH_2	Graphene functionalized with aminic group
GO	Graphene oxide
LbL	Layer-by-Layer

LGO	Large graphene oxide
PDI	Polydispersity index
PEI	Polyethyleneimine
rGO	Reduced graphene oxide
SGO	Small graphene oxide
UHV	Ultra-high vacuum
ULGO	Ultra-large graphene oxide
XPS	X-ray photoelectron spectroscopy
WCA	Water contact angle

References

1. Cherenack, K.; Zysset, C.; Kinkeldei, T.; Münzenrieder, N.; Tröster, G. Woven Electronic Fibers with Sensing and Display Functions for Smart Textiles. *Adv. Mater.* **2010**, *22*, 5178–5182. [CrossRef]
2. Geim, A.K.; Novoselov, K.S. The Rise of Graphene. *Nat. Mater.* **2007**, *6*, 183–191. [CrossRef] [PubMed]
3. Robert, C.; Feller, J.F.; Castro, M. Sensing Skin for Strain Monitoring Made of PC-CNT Conductive Polymer Nanocomposite Sprayed Layer by Layer. *ACS Appl. Mater. Interfaces* **2012**, *4*, 3508–3516. [CrossRef]
4. Sahito, I.A.; Sun, K.C.; Arbab, A.A.; Qadir, M.B.; Jeong, S.H. Graphene Coated Cotton Fabric as Textile Structured Counter Electrode for DSSC. *Electrochim. Acta* **2015**, *173*, 164–171. [CrossRef]
5. Ma, B.; Rodriguez, R.D.; Ruban, A.; Pavlov, S.; Sheremet, E. The Correlation between Electrical Conductivity and Second-Order Raman Modes of Laser-Reduced Graphene Oxide. *Phys. Chem. Chem. Phys.* **2019**, *21*, 10125–10134. [CrossRef]
6. Childres, I.; Jauregui, L.A.; Park, W.; Cao, H.; Chen, Y.P. Raman Spectroscopy of Graphene and Related Materials. In *New Developments in Photon and Materials Research*; Jang, J.I., Ed.; Physics Research and Technology, Materials Science and Technologies; Nova Science Publishers Inc.: New York, NY, USA, 2013.
7. Krishna, D.N.G.; Philip, J. Review on Surface-Characterization Applications of X-Ray Photoelectron Spectroscopy (XPS): Recent Developments and Challenges. *Appl. Surf. Sci. Adv.* **2022**, *12*, 100332. [CrossRef]
8. Wu, J.-B.; Lin, M.-L.; Cong, X.; Liu, H.-N.; Tan, P.-H. Raman Spectroscopy of Graphene-Based Materials and Its Applications in Related Devices. *Chem. Soc. Rev.* **2018**, *47*, 1822–1873. [CrossRef] [PubMed]
9. Jia, X.; Campos-Delgado, J.; Terrones, M.; Meunier, V.; Dresselhaus, M.S. Graphene Edges: A Review of Their Fabrication and Characterization. *Nanoscale* **2011**, *3*, 86–95. [CrossRef]
10. Choudhary, F.; Mudgal, P.; Parvez, A.; Sharma, P.; Farooqi, H. A Review on Synthesis, Properties and Prospective Applications of Carbon Nanomaterials. *Nano-Struct. Nano-Objects* **2024**, *38*, 101186. [CrossRef]
11. Gulia, S.; Moniruzzaman, M.; Panda, A. Approaches in Graphene-Based Nanocomposites: Synthesis, Modification, and Multi-faceted Applications. *FlatChem* **2024**, *48*, 100761. [CrossRef]
12. Wang, H.; Wang, H.S.; Ma, C.; Chen, L.; Jiang, C.; Chen, C.; Xie, X.; Li, A.-P.; Wang, X. Graphene Nanoribbons for Quantum Electronics. *Nat. Rev. Phys.* **2021**, *3*, 791–802. [CrossRef]
13. Cai, G.; Xu, Z.; Yang, M.; Tang, B.; Wang, X. Functionalization of Cotton Fabrics through Thermal Reduction of Graphene Oxide. *Appl. Surf. Sci.* **2017**, *393*, 441–448. [CrossRef]
14. Karim, N.; Afroj, S.; Tan, S.; He, P.; Fernando, A.; Carr, C.; Novoselov, K.S. Scalable Production of Graphene-Based Wearable e-Textiles. *ACS Nano* **2017**, *11*, 12266–12275. [CrossRef]
15. Liu, Y.; Fei, B.; Xin, J.H. Functionalization of Fabrics with Graphene-Based Coatings: Mechanisms, Approaches, and Functions. *Coatings* **2023**, *13*, 1580. [CrossRef]
16. Makowski, T.; Svyntkivska, M.; Piorkowska, E.; Mizerska, U.; Fortuniak, W.; Kowalczyk, D.; Brzezinski, S. Conductive and Superhydrophobic Cotton Fabric through Pentaerythritol Tetrakis(3-(3,5-Di-Tert-Butyl-4-Hydroxyphenyl)Propionate) Assisted Thermal Reduction of Graphene Oxide and Modification with Methyltrichlorosilane. *Cellulose* **2018**, *25*, 5377–5388. [CrossRef]
17. Neves, A.I.S.; Bointon, T.H.; Melo, L.V.; Russo, S.; de Schrijver, I.; Craciun, M.F.; Alves, H. Transparent Conductive Graphene Textile Fibers. *Sci. Rep.* **2015**, *5*, 9866. [CrossRef]
18. Tang, X.; Tian, M.; Qu, L.; Zhu, S.; Guo, X.; Han, G.; Sun, K.; Hu, X.; Wang, Y.; Xu, X. Functionalization of Cotton Fabric with Graphene Oxide Nanosheet and Polyaniline for Conductive and UV Blocking Properties. *Synth. Met.* **2015**, *202*, 82–88. [CrossRef]
19. Zhang, Y.; Zhang, G.; Dong, Y.; Wu, Y.; Yu, L.; Bai, Y. Interfacial Modulation of Polydopamine–Reduced Graphene Oxide for Achieving Highly Conductive and Strong Graphene/Cotton Composite Yarn Toward Smart Wearable Devices. *Adv. Fiber Mater.* **2024**, *6*, 1798–1812. [CrossRef]
20. Zhang, L.; Zhao, Y.; Yu, H.; Chen, L.; Liu, X.; Zhang, A.; Deng, Z.; Ou, J.Z. Sub-Nano Porous Graphene-Based Membranes Enabled by In-Situ-Grown ZIF-8 for Enhanced CO_2 Capture. *Chem. Eng. J.* **2024**, *494*, 153250. [CrossRef]

21. Mazurkiewicz-Pawlicka, M.; Nowak, M.; Malolepszy, A.; Witowski, A.; Wasik, D.; Hu, Y.; Stobinski, L. Graphene Oxide with Controlled Content of Oxygen Groups as a Filler for Polymer Composites Used for Infrared Radiation Shielding. *Nanomaterials* **2020**, *10*, 32. [CrossRef]
22. McCreary, A.; An, Q.; Forster, A.M.; Liu, K.; He, S.; Macosko, C.W.; Stein, A.; Hight Walker, A.R. Raman Imaging of Surface and Sub-Surface Graphene Oxide in Fiber Reinforced Polymer Nanocomposites. *Carbon* **2019**, *143*, 793–801. [CrossRef]
23. Jin, H.; Zhu, L.; Jin, S.; Jiang, L.; Zou, Y. Raman Spectroscopy Analysis of Graphene Oxide-Enhanced Textiles. *J. Raman Spectrosc.* **2021**, *52*, 843–848. [CrossRef]
24. Attari, K.; Shekarriz, S.; Montazer, M.; Shariatinia, Z.; Mokhtari, J. Applications of Graphene, Graphene Oxide, and Reduced Graphene Oxide on Cotton Fabric. *Cellulose* **2025**, *32*, 5795–5839. [CrossRef]
25. Bellier, N.; Baipaywad, P.; Ryu, N.; Lee, J.Y.; Park, H. Recent Biomedical Advancements in Graphene Oxide- and Reduced Graphene Oxide-Based Nanocomposite Nanocarriers. *Biomater. Res.* **2022**, *26*, 65. [CrossRef]
26. Rahman, M.M.; Hossen, S.; Sarkar, B.; Rahman, M.T.; Lee, S.C.; Jung, Y.; Shim, J.S. High Density 3D-Structured Graphene for Long-Life and High Energy Density Lithium-Ion Battery. *J. Power Sources* **2025**, *650*, 237493. [CrossRef]
27. Rahman, M.M.; Rahman, M.T.; Hossen, S.; Sarkar, B.; Lee, S.C.; Jung, Y.; Shim, J.S. Polyethersulfone-Based Thick Polymer-Supported Graphene Sheet for High Energy Density Lithium-Ion Battery. *J. Power Sources* **2025**, *626*, 235774. [CrossRef]
28. Rahman, M.M.; Sarkar, B.; Rahman, M.T.; Jin, G.J.; Uddin, M.J.; Bhuiyan, N.H.; Shim, J.S. Development of a Highly Sensitive CNT-Metal Graphene Hybrid Nano-IDA Electrochemical Biosensor for the Diagnosis of Alzheimer's Disease. *Biomater. Sci.* **2024**, *12*, 5203–5214. [CrossRef]
29. Mizerska, U.; Fortuniak, W.; Makowski, T.; Svyntkivska, M.; Piorkowska, E.; Kowalczyk, D.; Brzezinski, S.; Kregiel, D. Antibacterial Electroconductive RGO Modified Cotton Fabric. *Polym. Adv. Technol.* **2021**, *32*, 3975–3981. [CrossRef]
30. Mohan, V.B.; Brown, R.; Jayaraman, K.; Bhattacharyya, D. Characterisation of Reduced Graphene Oxide: Effects of Reduction Variables on Electrical Conductivity. *Mater. Sci. Eng. B* **2015**, *193*, 49–60. [CrossRef]
31. Li, Q.; Zong, Y.; Jiang, Y.; Zhang, J.; Zhao, R.; Chen, J.; Shi, Y.; Tan, L. Functionalization of Cotton Fabrics through PEI/PA/FeAl Ternary System with Enhanced Flame Retardance and Antibacterial Properties. *Cellulose* **2024**, *31*, 6517–6533. [CrossRef]
32. Wågberg, L. Polyelectrolyte Adsorption onto Cellulose Fibres—A Review. *Nord. Pulp Pap. Res. J.* **2001**, *15*, 586–597. [CrossRef]
33. Pan, Y.; Fu, L.; Du, J.; Zhang, D.; Lü, T.; Zhang, Y.; Zhao, H. Layer-by-Layer Self-Assembly Coating for Multi-Functionalized Fabrics: A Scientometric Analysis in CiteSpace (2005–2021). *Molecules* **2022**, *27*, 6767. [CrossRef] [PubMed]
34. Ariga, K.; Lvov, Y.; Decher, G. There Is Still Plenty of Room for Layer-by-Layer Assembly for Constructing Nanoarchitectonics-Based Materials and Devices. *Phys. Chem. Chem. Phys.* **2022**, *24*, 4097–4115. [CrossRef]
35. Fan, F.; Zhou, C.; Wang, X.; Szpunar, J. Layer-by-Layer Assembly of a Self-Healing Anticorrosion Coating on Magnesium Alloys. *ACS Appl. Mater. Interfaces* **2015**, *7*, 27271–27278. [CrossRef]
36. Zhao, X.; Jin, Z.; Zhang, B.; Zhai, X.; Liu, S.; Sun, X.; Zhu, Q.; Hou, B. Effect of Graphene Oxide on Anticorrosion Performance of Polyelectrolyte Multilayer for 2A12 Aluminum Alloy Substrates. *RSC Adv.* **2017**, *7*, 33764–33774. [CrossRef]
37. Tian, M.; Hu, X.; Qu, L.; Du, M.; Zhu, S.; Sun, Y.; Han, G. Ultraviolet Protection Cotton Fabric Achieved via Layer-by-Layer Self-Assembly of Graphene Oxide and Chitosan. *Appl. Surf. Sci.* **2016**, *377*, 141–148. [CrossRef]
38. Badawi, N.M.; Batoo, K.M.; Hussain, S.; Agrawal, N.; Bhuyan, M.; Bashir, S.; Subramaniam, R.; Kasi, R. Design and Characterization of Electroconductive Graphene-Coated Cotton Fabric for Wearable Electronics. *Coatings* **2023**, *13*, 1601. [CrossRef]
39. Kwame Fobiri, G.; Eghan, B.; Kanyire Seidu, R.; Tawiah, B. A Review of Functionalized Graphene-Oxide in Wearable Textile Sensors and Supercapacitors for Biomedical Applications. *Essent. Chem* **2025**, *2*, 2493111. [CrossRef]
40. Tartaglia, E.; Moglianetti, M.; Caminati, G.; Travaglia, A.; Zanardi, C.; Baglioni, P.; Galvagno, E.; Menegazzo, F. Processo per La Copertura Di Manufatti Con Ossido Di Grafene. Italy Patent Application 102025000008268, 14 April 2025.
41. Choi, H.J.; Ko, M.; Kim, I.H.; Yu, H.; Kim, J.Y.; Yun, T.; Yang, J.S.; Yang, G.G.; Jeong, H.S.; Moon, M.H.; et al. Wide-Range Size Fractionation of Graphene Oxide by Flow Field-Flow Fractionation. *ACS Nano* **2022**, *16*, 9172–9182. [CrossRef]
42. Tartaglia, E.; Forti, S.; Galeotti, M.; Porcinai, S.; Cagnini, A.; Ricotta, N.; Puppulin, L.; Lauciello, S.; Marras, S.; Baglioni, P.; et al. Edge-to-Edge Assembly of Graphene Oxide Flakes as Nanometric Anticorrosive Barriers for Heritage Metals. *ACS Appl. Nano Mater.* **2026**, *9*, 6104–6118. [CrossRef]
43. Orlando, A.; Franceschini, F.; Muscas, C.; Pidkova, S.; Bartoli, M.; Rovere, M.; Tagliaferro, A. A Comprehensive Review on Raman Spectroscopy Applications. *Chemosensors* **2021**, *9*, 262. [CrossRef]
44. Casiraghi, C.; Hartschuh, A.; Qian, H.; Pliscanec, S.; Georgia, C.; Fasoli, A.; Novoselov, K.S.; Basko, D.M.; Ferrari, A.C. Raman Spectroscopy of Graphene Edges. *Nano Lett.* **2009**, *9*, 1433–1441. [CrossRef]
45. Casiraghi, C.; Pisana, S.; Novoselov, K.S.; Geim, A.K.; Ferrari, A.C. Raman Fingerprint of Charged Impurities in Graphene. *Appl. Phys. Lett.* **2007**, *91*, 233108. [CrossRef]
46. Ferrari, A.C.; Meyer, J.C.; Scardaci, V.; Casiraghi, C.; Lazzeri, M.; Mauri, F.; Piscanec, S.; Jiang, D.; Novoselov, K.S.; Roth, S.; et al. Raman Spectrum of Graphene and Graphene Layers. *Phys. Rev. Lett.* **2006**, *97*, 187401. [CrossRef] [PubMed]

47. Ferrari, A.C. Raman Spectroscopy of Graphene and Graphite: Disorder, Electron–Phonon Coupling, Doping and Nonadiabatic Effects. *Solid State Commun.* **2007**, *143*, 47–57. [CrossRef]
48. Das, A.; Pisana, S.; Chakraborty, B.; Piscanec, S.; Saha, S.K.; Waghmare, U.V.; Novoselov, K.S.; Krishnamurthy, H.R.; Geim, A.K.; Ferrari, A.C.; et al. Monitoring Dopants by Raman Scattering in an Electrochemically Top-Gated Graphene Transistor. *Nat. Nanotechnol.* **2008**, *3*, 210–215. [CrossRef] [PubMed]
49. Ferralis, N.; Maboudian, R.; Carraro, C. Evidence of Structural Strain in Epitaxial Graphene Layers on 6H-SiC(0001). *Phys. Rev. Lett.* **2008**, *101*, 156801. [CrossRef]
50. Mohiuddin, T.M.G.; Lombardo, A.; Nair, R.R.; Bonetti, A.; Savini, G.; Jalil, R.; Bonini, N.; Basko, D.M.; Galiotis, C.; Marzari, N.; et al. Uniaxial Strain in Graphene by Raman Spectroscopy: G Peak Splitting, Grüneisen Parameters, and Sample Orientation. *Phys. Rev. B* **2009**, *79*, 205433. [CrossRef]
51. Banhart, F.; Kotakoski, J.; Krasheninnikov, A.V. Structural Defects in Graphene. *ACS Nano* **2011**, *5*, 26–41. [CrossRef]
52. Boukhvalov, D.W.; Katsnelson, M.I. Chemical Functionalization of Graphene with Defects. *Nano Lett.* **2008**, *8*, 4374–4379. [CrossRef]
53. Eckmann, A.; Felten, A.; Mishchenko, A.; Britnell, L.; Krupke, R.; Novoselov, K.S.; Casiraghi, C. Probing the Nature of Defects in Graphene by Raman Spectroscopy. *Nano Lett.* **2012**, *12*, 3925–3930. [CrossRef]
54. Malard, L.M.; Pimenta, M.A.; Dresselhaus, G.; Dresselhaus, M.S. Raman Spectroscopy in Graphene. *Phys. Rep.* **2009**, *473*, 51–87. [CrossRef]
55. Tuinstra, F.; Koenig, J.L. Raman Spectrum of Graphite. *J. Chem. Phys.* **1970**, *53*, 1126–1130. [CrossRef]
56. López-Díaz, D.; López Holgado, M.; García-Fierro, J.L.; Velázquez, M.M. Evolution of the Raman Spectrum with the Chemical Composition of Graphene Oxide. *J. Phys. Chem. C* **2017**, *121*, 20489–20497. [CrossRef]
57. Roy Choudhury, A.K. Pre-Treatment and Preparation of Textile Materials Prior to Dyeing. In *Handbook of Textile and Industrial Dyeing*; Clark, M., Ed.; Woodhead Publishing Series in Textiles; Woodhead Publishing: Cambridge, UK, 2011; Volume 1, pp. 64–149.
58. Hassabo, A.G.; Mendrek, A.; Popescu, C.; Keul, H.; Möller, M. Deposition of Functionalized Polyethylenimine-Dye onto Cotton and Wool Fibres. *Res. J. Text. Appar.* **2014**, *18*, 36–49. [CrossRef]
59. Wojdyr, M. Fityk: A General-Purpose Peak Fitting Program. *J. Appl. Crystallogr.* **2010**, *43*, 1126–1128. [CrossRef]
60. Ferrari, A.C.; Robertson, J. Interpretation of Raman Spectra of Disordered and Amorphous Carbon. *Phys. Rev. B* **2000**, *61*, 14095–14107. [CrossRef]
61. Paris, O.; Zollfrank, C.; Zickler, G.A. Decomposition and Carbonisation of Wood Biopolymers—A Microstructural Study of Softwood Pyrolysis. *Carbon* **2005**, *43*, 53–66. [CrossRef]
62. Yamauchi, S.; Kurimoto, Y. Raman Spectroscopic Study on Pyrolyzed Wood and Bark of Japanese Cedar: Temperature Dependence of Raman Parameters. *J. Wood Sci.* **2003**, *49*, 235–240. [CrossRef]
63. Zickler, G.A.; Smarsly, B.; Gierlinger, N.; Peterlik, H.; Paris, O. A Reconsideration of the Relationship between the Crystallite Size La of Carbons Determined by X-Ray Diffraction and Raman Spectroscopy. *Carbon* **2006**, *44*, 3239–3246. [CrossRef]
64. Sadezky, A.; Muckenhuber, H.; Grothe, H.; Niessner, R.; Pöschl, U. Raman Microspectroscopy of Soot and Related Carbonaceous Materials: Spectral Analysis and Structural Information. *Carbon* **2005**, *43*, 1731–1742. [CrossRef]
65. Shirley, D.A. High-Resolution X-Ray Photoemission Spectrum of the Valence Bands of Gold. *Phys. Rev. B* **1972**, *5*, 4709–4714. [CrossRef]
66. Susi, T.; Pichler, T.; Ayala, P. X-Ray Photoelectron Spectroscopy of Graphitic Carbon Nanomaterials Doped with Heteroatoms. *Beilstein J. Nanotechnol.* **2015**, *6*, 177–192. [CrossRef]
67. Rodriguez-Loya, J.; Lerma, M.; Gardea-Torresdey, J.L. Dynamic Light Scattering and Its Application to Control Nanoparticle Aggregation in Colloidal Systems: A Review. *Micromachines* **2023**, *15*, 24. [CrossRef]
68. Pimenta, M.A.; Dresselhaus, G.; Dresselhaus, M.S.; Cançado, L.G.; Jorio, A.; Saito, R. Studying Disorder in Graphite-Based Systems by Raman Spectroscopy. *Phys. Chem. Chem. Phys.* **2007**, *9*, 1276–1290. [CrossRef]
69. Cançado, L.G.; Jorio, A.; Ferreira, E.H.M.; Stavale, F.; Achete, C.A.; Capaz, R.B.; Moutinho, M.V.O.; Lombardo, A.; Kulmala, T.S.; Ferrari, A.C. Quantifying Defects in Graphene via Raman Spectroscopy at Different Excitation Energies. *Nano Lett.* **2011**, *11*, 3190–3196. [CrossRef] [PubMed]
70. López-Díaz, D.; Delgado-Notario, J.A.; Clericò, V.; Diez, E.; Merchán, M.D.; Velázquez, M.M. Towards Understanding the Raman Spectrum of Graphene Oxide: The Effect of the Chemical Composition. *Coatings* **2020**, *10*, 524. [CrossRef]
71. King, A.A.K.; Davies, B.R.; Noorbehesht, N.; Newman, P.; Church, T.L.; Harris, A.T.; Razal, J.M.; Minett, A.I. A New Raman Metric for the Characterisation of Graphene Oxide and Its Derivatives. *Sci. Rep.* **2016**, *6*, 19491. [CrossRef]
72. Shen, Y.; Yang, S.; Zhou, P.; Sun, Q.; Wang, P.; Wan, L.; Li, J.; Chen, L.; Wang, X.; Ding, S.; et al. Evolution of the Band-Gap and Optical Properties of Graphene Oxide with Controllable Reduction Level. *Carbon* **2013**, *62*, 157–164. [CrossRef]
73. Venezuela, P.; Lazzeri, M.; Mauri, F. Theory of Double-Resonant Raman Spectra in Graphene: Intensity and Line Shape of Defect-Induced and Two-Phonon Bands. *Phys. Rev. B* **2011**, *84*, 035433. [CrossRef]

74. del Corro, E.; Taravillo, M.; González, J.; Baonza, V.G. Raman Characterization of Carbon Materials under Non-Hydrostatic Conditions. *Carbon* **2011**, *49*, 973–979. [CrossRef]
75. Liu, C.; Liu, H.; Lu, C.; Tang, K.; Zhang, Y. Polyethyleneimine-Modified Graphene Oxide/PNIPAm Thermoresponsive Hydrogels with Rapid Swelling/Deswelling and Improved Mechanical Properties. *J. Mater. Sci.* **2017**, *52*, 11715–11724. [CrossRef]
76. Vitorino, L.S.; dos Santos, T.C.; Bessa, I.A.A.; Santos, E.C.S.; Verçoza, B.R.F.; de Oliveira, L.A.S.; Rodrigues, J.C.F.; Ronconi, C.M. Amphotericin-B-Loaded Polymer-Functionalized Reduced Graphene Oxides for Leishmania Amazonensis Chemo-Photothermal Therapy. *Colloids Surf. B Biointerfaces* **2022**, *209*, 112169. [CrossRef]
77. Muthu, R.N.; Rajashabala, S.; Kannan, R. Synthesis and Characterization of Microporous Hybrid Nanocomposite Membrane as Potential Hydrogen Storage Medium towards Fuel Cell Applications. *Ionics* **2019**, *25*, 3561–3575. [CrossRef]